Three-dimensional Study of Compressed Gas Diffusion Layers using Synchrotron X-ray Imaging

C. Tötzke[a, b], G. Gaiselmann[c], M. Osenberg[b], J. Bohner[d], T. Arlt[b], H. Markötter[b], A. Hilger[b], F. Wieder[a, b], A. Kupsch[e], B.R. Müller[e] , M.P. Hentschel[e], J. Banhart[a, b], V. Schmidt[c], W. Lehnert[d,f] and I. Manke[b]

[a] Technische Universität Berlin, 10623 Berlin, Germany
[b] Helmholtz-Zentrum Berlin für Materialien und Energie, 14109 Berlin, Germany
[c] Universität Ulm, 89069 Ulm, Germany
[d] Forschungszentrum Jülich, 52425 Jülich, Germany
[e] BAM Bundesanstalt für Materialforschung und –prüfung, 12200 Berlin, Germany
[f] RWTH Aachen University, 52056 Aachen, Germany

We present a synchrotron X-ray tomographic study on the morphology of carbon fiber-based gas diffusion layer (GDL) material under compression. A dedicated compression device is used to provide well defined compression conditions. A flat compression punch is employed to study the fiber geometry at different degrees of compression. Transport relevant geometrical parameters such as porosity, pore size and tortuosity distributions are calculated. The geometric properties notably change upon compression which has direct impact on transport conditions for gas and fluid flow. The availability of broad 3D paths, which are most important for the transport of liquid water from the catalyst layer through the GDL, is markedly reduced after compression. In a second experiment, we study the influence of the channel-land-pattern of the flow-field on shape and microstructure of the GDL. A flow-field compression punch is employed to reproduce the inhomogeneous compression conditions found during fuel cell assembly. While homogenously compressed underneath the land the GDL is much less and inhomogeneously compressed under the channel. The GDL material extends far into the channel volume where it can considerably influence gas and fluid flow. Loose fiber endings penetrate deeply into the channel and form obstacles for the discharge of liquid water droplets.

1. Introduction

Gas diffusion layers (GDLs) play a key role for the efficient operation of fuel cells. The water management of proton-exchange fuel cells (PEFCs) crucially relies on both water and media transport inside the gas diffusion layers. Common GDL types consist of porous carbon fiber-based materials that allow for a concurrent transfer of gaseous reactants from the flow-field channels to the electrodes and an effective removal of liquid water produced at the catalyst layer. Furthermore, the GDL must keep the membrane humidified to maintain its proton conductivity [1-3]. Therefore, an important design requirement of GDL materials is a careful adjustment of water transport and storage capacities. Numerous theoretical [4-8] and experimental [9, 10] studies focusing on two-phase flow in porous media contributed to the basic understanding of underlying water transport mechanisms. Recently, neutron [11, 12] and X-ray imaging [13-17] were shown to be well suited for the investigation of water in porous materials such as GDLs [18-28]. The transport properties of GDLs are closely linked to their microstructure. Therefore, a precise knowledge of the three-dimensional morphology is a basic prerequisite to understand the functionality of GDLs.

A sophisticated way of systematically designing GDL materials is to detect microstructures with improved physical properties by means of model-based computer experiments. The development of appropriate stochastic microstructure models allows one to create virtual 3D structures, the transport properties of which are subsequently evaluated by means of numerical transport simulations. Systematic parameter modification of the microstructure model together with numerical transport simulation can help to identify most suitable transport geometries [29]. The combination of 3D analysis, geometric modeling [30, 31] and transport simulation [32, 33] is considered a promising approach to establish a sound basis for systematic virtual design of fiber-based porous microstructures.

We performed high-resolution synchrotron X-ray measurements on various GDL materials at different degrees of compression. This broad experimental data set serves as input for the development and validation of stochastic microstructure models. In this paper, we focus on the nonwoven fiber-based material H2315 produced by Freudenberg FFCCT.

2. Methods and Materials

2.1. Imaging conditions

The experiments were performed at the Helmholtz-Zentrum Berlin using the synchrotron tomography station of the BAMline which is located at the synchrotron source BESSY II (Berlin/Germany) [34] . The principal set-up of the tomographic measurement is displayed in figure 1.

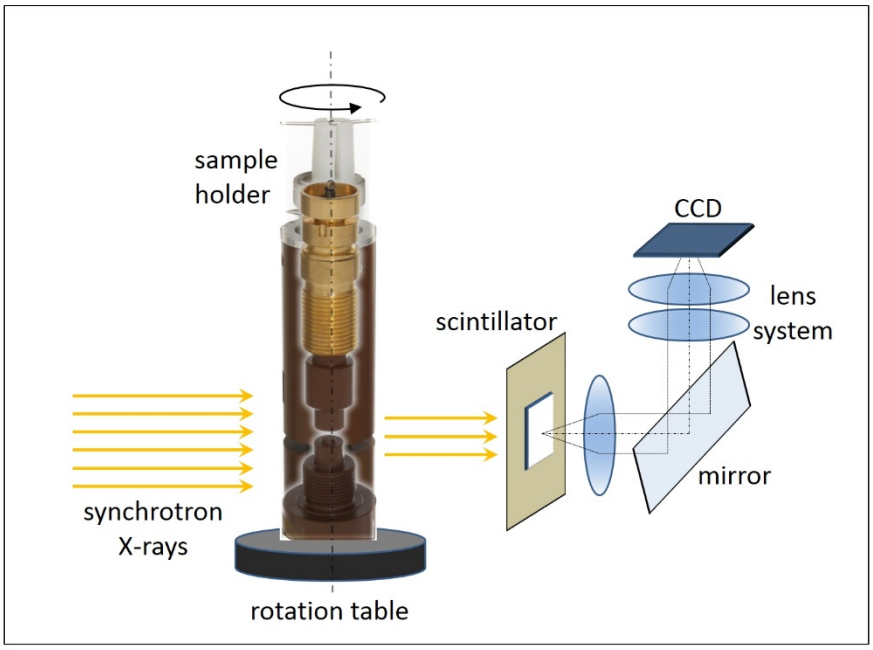

Figure 1. Scheme of the principal experimental set-up of the tomographic instrument.

A W-Si multilayer monochromator was employed to turn the white beam into monochromatic X-ray light with an energy resolution of $\Delta E/E=10^{-2}$. The beam energy was adjusted to 15 keV in order to achieve optimal contrast for fibers. A PCO camera (4008×2672 pixel^2) in combination with a lens system and a CWO scintillator screen was use to capture a field of view of 3.6×2.3 mm^2 which corresponds to an image pixel size of 0.876 µm and a respective physical spatial resolution of about 2 µm [35]. Circular GDL samples of 3mm diameter were aligned by the sample holder and mounted on a translation/rotation unit. For each tomogram, a sample was rotated stepwise over an angular range of 180°. A radiographic set of 1500 projections and 500 flatfield images was acquired and subsequently reconstructed to a 3D image volume. The exposure time was 2.5 s plus 1.7 s read-out time for a single radiograph adding up to an acquisition time of 140 min for an entire tomogram.

2.2. Sample compression device

High-resolution synchrotron studies on compressed microstructures of fuel cell components such as GDL or membrane electrode assemblies call for a dedicated compression device that ensures well-defined compression conditions during tomographic measurements. The design of this device must allow for both planar and horizontal alignment of a sample and precise adjustment of its thickness with an accuracy of a few micrometers. In order to create different compression conditions the device is equipped with differently shaped compression punches: A flat punch realizes homogenous compression while a punch with an integrated channel profile simulates the inhomogeneous compression exerted by the flow-field during fuel cell assembly which gives rise to an embossed channel-rip-pattern. Moreover, some instrumental requirements have to be taken into account: sufficient beam transmittance has to be ensured, dimensional restrictions with respect to the small field of view apply (usually some millimeters at a spatial resolution of about 1 µm), and mechanical stability is required in order to keep the sample at rest during tomographic scans.

In order to satisfy these requirements a dedicated compression device has been designed and constructed at the Forschungszentrum Jülich. It facilitates tomographic *ex situ* measurements of GDL components, such as GDL or membrane electrolyte assemblies at the synchrotron. Due to its chemical insensitivity, e.g. to acids, the device can be also used to study components of high-temperature PEM fuel cells which contain phosphoric acid [36-38].

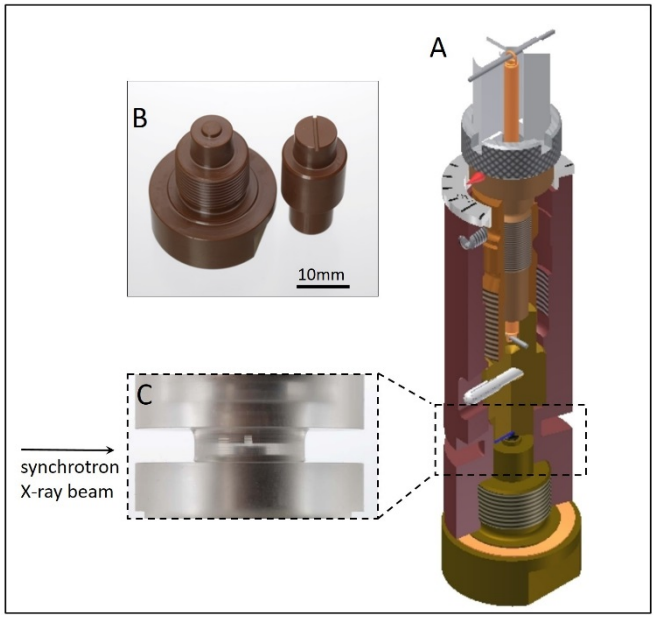

Figure 2. Compression device used for high-resolution tomography of circular GDL samples. A: perspective view showing the interior construction of the device. B: Sample holder basis (left) and compression cylinder with integrated flow-field channel geometry (right). C: Detail of the sample bearing section.

Figure 2 illustrates the principal design of the compression device. The base of the device is depicted in figure 2C (left). It features a platform on which the circular sample is placed on. The main compression unit including the adjustable compression tool is fastened to the top of the base element. This design facilitates quick and easy exchange of samples which helps to save valuable beamtime at the electron storage ring. An adjusting screw with an ultra-fine-pitch thread allows for a vertical adjustment of the compression punch with a precision of about ± 5 µm. The compression punch does not twist during vertical adjustment, thus providing a torsion-free sample compression. Relative vertical displacements can be read from a scale visually, while the absolute position of the punch is verified by analyzing the radiographs. Within the field of view the device is made of the durable high-performance polyimide-based polymer Vespel® with a reduced wall thickness of 1 mm which ensures high beam transmission.

The compression unit is equipped with exchangeable compression tools: a flat punch generates homogenous compression and a flow-field punch is used to simulate inhomogeneous compression conditions as found in assembled fuel cells. The latter punch features a 0.8 mm wide and 1 mm deep channel profile (see figure 2 B right).

2.3. Materials

The present tomographic study covers a range of different GDL materials measured at four stages of increasing compression. In this paper, we focus on the GDL type H2315 which is a nonwoven, carbon fiber-based felt material produced by the company Freudenberg FFCCT. This basis material is used as a standard GDL in many fuel cells where its physical properties are adopted to the requirements of the respective application, e.g. by adding water proofing compounds and/or a microporous layer (MPL).

3. Results and Discussion

In this section the microstructure of GDL samples compressed by both a flat and by a flow-field punch is analyzed at four stages of increasing compression (about 0 vol.%, 10 vol.%, 20 vol.%, and 30 vol.%).

3.1. Homogenous compression

In figure 3 the morphology of the homogenously compressed GDL sample is rendered in an area of 1000 × 1000 µm^2. Using the compression device, the initial thickness of the sample Z_0 = 223 µm is successively reduced to Z_{10} = 203 µm, Z_{20} = 176 µm, Z_{30} = 154 µm, which corresponds to an actual degree of compression of 9 vol.%, 21 vol.%, 31 vol.%, respectively. We refer to the initial thickness Z_0 as "uncompressed state" even though it actually includes a precompression of about 0.025 MPa, which is necessary to create a plain sample orientation and a smooth GDL surface which is needed to be able to determine the initial GDL thickness. As apparent in figure 3 the tomographic data is sufficiently well resolved to clearly follow the course of single fibers and to distinguish between fibers even if they are located very close to each other. A comparison of the 3D images shows that the compression of the GDL material takes place at the expense of the pore volume. No notable lateral dilatation of sample was observed, suggesting that fibers are almost exclusively translated in the *z*-direction of compression.

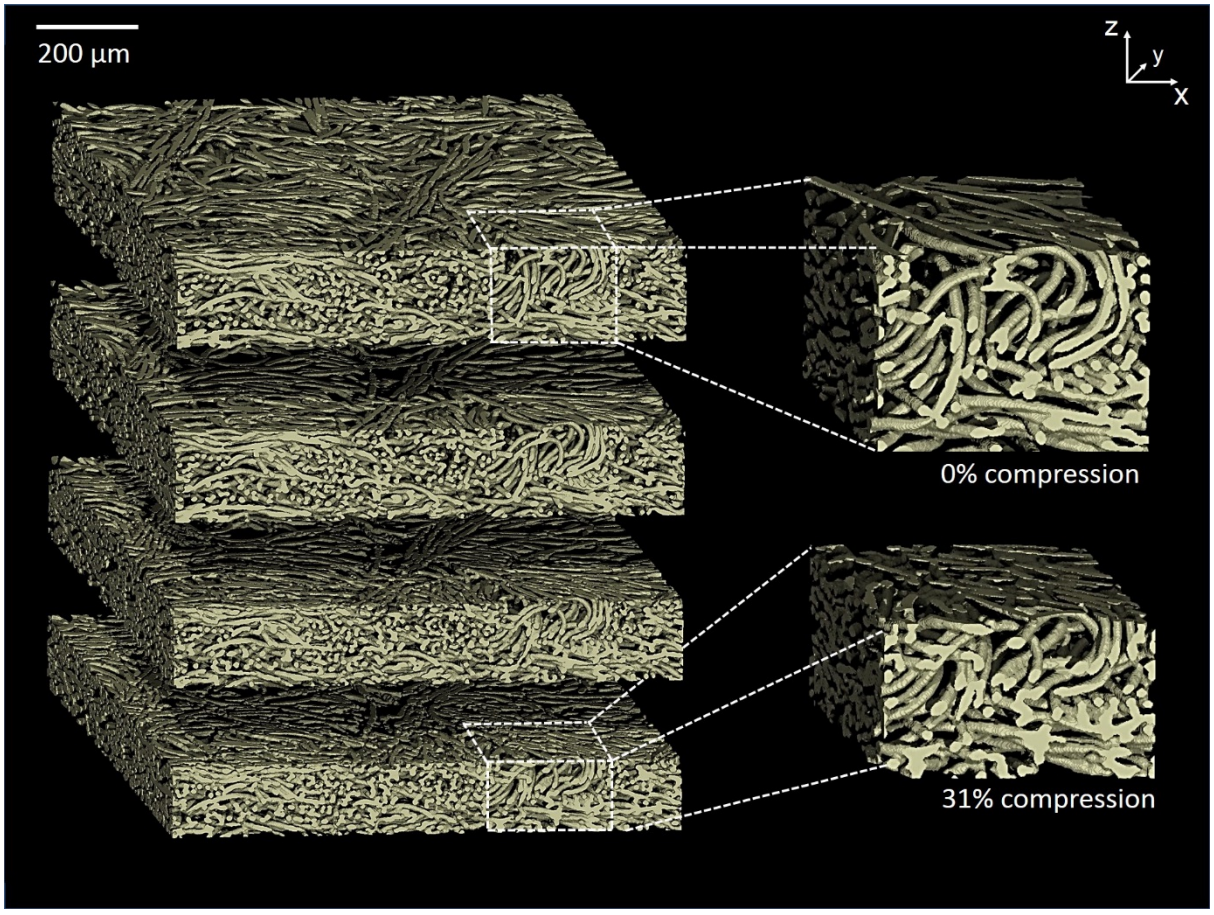

Figure 3. 3D representation of a nonwoven GDL sample (type Freudenberg H2315) at different rates of compression 0%, 09%, 21%, 31% (from top to bottom), sample is rendered in an area of 1 × 1 mm^2.

In order to analyze the influence of compression on microstructural characteristics we computed the porosity, pore size distribution (PSD) and geometrical tortuosity of the material for different degrees of compression. Figure 4a shows that the initial porosity of about 78% of the uncompressed material decreases to 67% at a compression rate of 31%, which expresses the fact that only the pore volume is reduced whereas the fiber volume remains constant.

Another characteristic of porous materials is the PSD. In fiber structures, the entire pore space is interconnected and cannot be segmented into individual pores due to the lack of a physical criterion. For this reason, we analyze the pore structure in terms of the continuous pore size distribution (cPSD), which does not consider pores as discrete objects but treats the entire pore structure as continuum. The cPSD describes the pore volume P(r) that can be covered by spheres with a radius r, such that theses spheres do not overlap with the solid (fiber) phase. P(r) is calculated as a normalized volume with respect to the entire volume and, therefore, $\lim_{r\to 0} P(r)$ = porosity. For a more detailed mathematical description of the cPSD we refer to [39]. Figure 4b demonstrates that the compression of the GDL material results in a shift of the entire cPSD towards smaller pore radii. However, even at the highest degree of compression applied more than 25% of the total volume consists of pores with a radius of at least 10 µm. Pores larger than 30 µm can hardly be found for any of the compression states.

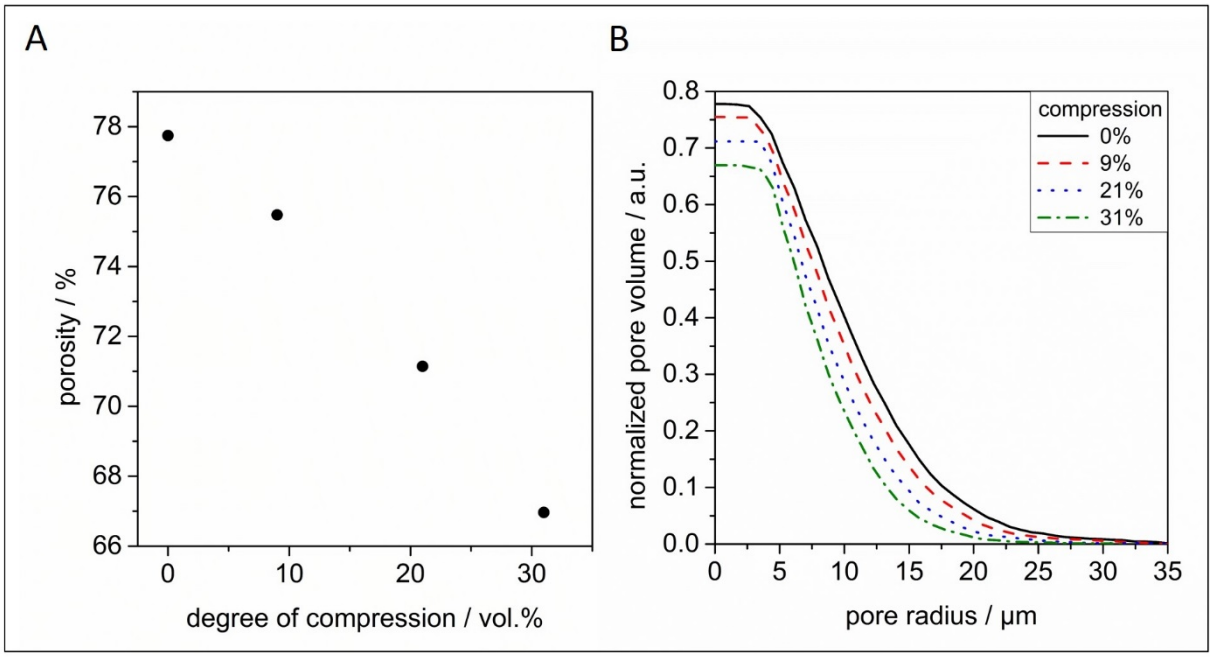

Figure 4. A: Porosity plotted against compression of the GDL. B: Plot of cPSD for different rates of compression. Values are calculated on an area of 700 × 700 µm^2.

In figure 5, the difference between the cPSD for the uncompressed sample and the one compressed by 31 vol.% is shown. Starting from large pore radii the difference in cPSD

increases. The maximum difference is found at a pore radius of about 10 µm, after which the difference decreases towards smaller radii. This proves that the compression of the pore phase occurs mostly at the expense of pores larger than R=10 µm. Naturally, smaller pores are also affected by compression. However, this is outweighed by the conversion of large pores into smaller ones. When considering pores ranging from 5 µm to 10 µm radius only, we find that such pores make up 31% of the total volume in the compressed and only 25% in the uncompressed state.

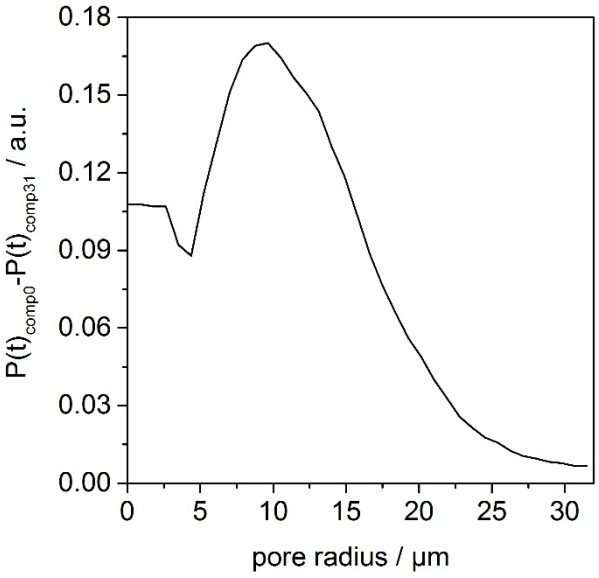

Figure 5. Difference in cPSD between the uncompressed sample and the one compressed by 31%.

Another important structural characteristics with respect to the transport of water and gas is the tortuosity of the pathways through the pore phase. We investigated the 'geometric tortuosity' of the pore space in through-plane direction, which is defined as the Euclidean length of the shortest paths along the edges of a geometric 3D graph representing all possible paths through the pore phase divided by the material thickness (in *z*-direction). Starting from a randomly chosen location on top of the porous material, its geometric tortuosity can be represented by a probability distribution instead of looking at the mean tortuosity only, see e.g. [31]. The geometric 3D graph of the pore phase is computed using the skeletonization algorithm implemented in the software Avizo 7. The results are given in table 1 and figure 6. The plots of geometric tortuosity distribution are quite similar at all considered degrees of compression. The mean tortuosity ranges between 1.42 and 1.50 and has no obvious correlation to the degree of compression. To better understand this observation it is useful to recall that the geometric evaluation of paths does not yet include a bottleneck criterion, i.e. the influence of minimum cross section on the transport capacity is not taken into account. The

course of the paths is determined by the skeletonization of the pore phase, i.e. the pathways follow the central axes of pores. Three-dimensional representations of percolation paths through the uncompressed and compressed material (see figure 6d) reveal that the straightness of the paths is very similar in either case. Figure 6b illustrates how a typical path has shrunk upon compression. As visible in figure 6c an original path might also be blocked by fibers displaced by compression, thus forcing an alternative transit pathway through the pore phase.

Table 1: Geometric tortuosity calculated in the through-plane direction.

compression [%]	through-plane connectivity	mean tortuosity	standard deviation
0	1	1,50	0,099
09	1	1,46	0,090
21	1	1,43	0,075
31	1	1,48	0,092

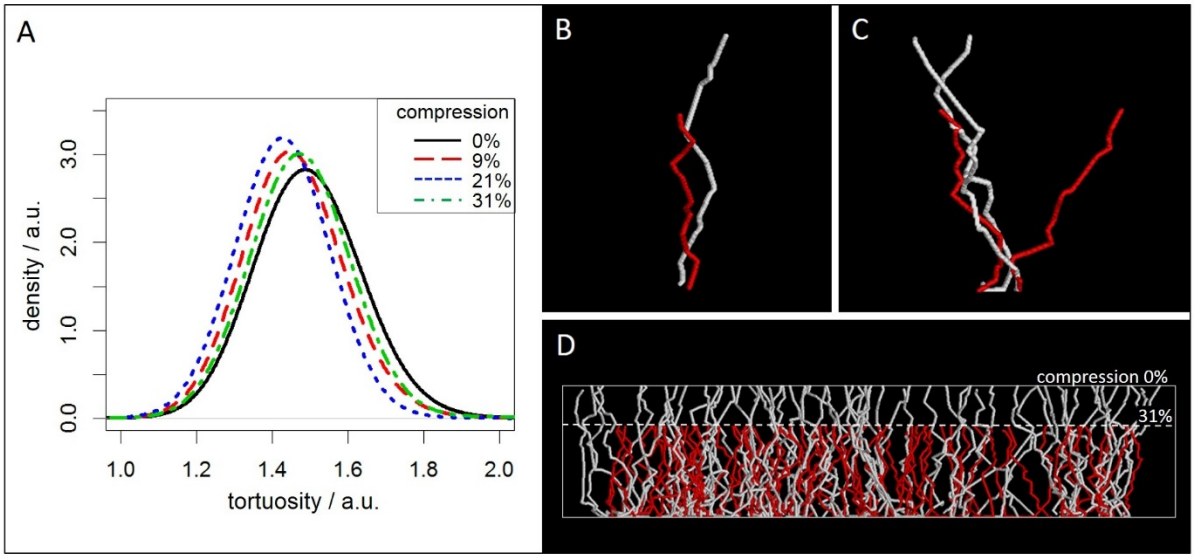

Figure 6. A: Distribution of geometric tortuosity for different degrees of compression; B-D: 3D representation of the percolation pathways through the pore phase for compression degrees of 0% und 31%. Compressed paths are plotted in red, uncompressed in white.

Taking into account the negligible transport capacity for liquid water of very narrow transport paths we extend the calculation of geometric tortuosity by introducing a bottleneck criterion. A minimum lateral distance R_{min} of the central axis of the pore and solid phase is required all along the pathway in order to be accepted as a path. In figure 7, the calculated mean geometric tortuosity in through-plane direction is displayed for three R_{min}: 1, 5 and 10 µm. The diagram also includes the through-plane connectivity of the paths, i.e. the probability that starting from a randomly chosen point at the surface a continuous pathway through the GDL

exists. In other words, we determine the shortest passage of a solid sphere of radius R_{min} through the GDL via the pore phase. The through-plane connectivity is the probability of a possible passage starting at a randomly chosen point of the surface. Figure 7a displays the results for the uncompressed material. It is obvious that the mean tortuosity increases with growing $R_{min.}$ If a minimum radius of 10 µm is assumed to be the smallest constriction along the 3D path through the GDL the mean tortuosity amounts to about 2.1, which is notably larger than the mean geometrical tortuosity of around 1.5 calculated for R_{min} = 1 µm. Furthermore, the plot of the through-plane connectivity reveals that liquid water transport through most pathways is limited by bottlenecks with a radius between 5-10 µm. While the probability of a possible transfer pathway for a solid sphere with radius R_{min} = 5 µm is still about 98% this probability drops to less than 6% for spheres with R_{min} = 10 µm. Figure 7b displays the results for the material compressed by 31 vol.%. Compression of the GDL aggravates transport limitations by bottlenecks: The through-plane connectivity decreases from 0.98 to 0.90 for R_{min} = 5 µm. For a radius constriction of R_{min} = 10 µm the connectivity even drops from 0.056 to 0.014. When comparing the mean tortuosity for R_{min} =10 µm in compressed and uncompressed states it appears that especially more tortuous paths are affected by the formation of bottlenecks with a radius < 10 µm.

The existence of a few wide paths is of great importance for the global liquid water transport. Due to their low transport resistance these paths provide preferred transfer routes for the removal of liquid water from the catalyst layer [8, 40]. In this study we focus on the through-plane tortuosity of the material. This property can be regarded as a material characteristic. The in-plane transport of water and gases in a cell is also important, especially under the lands. Due to the anisotropic nature of the GDL material, the in-plane tortuosity would differ.

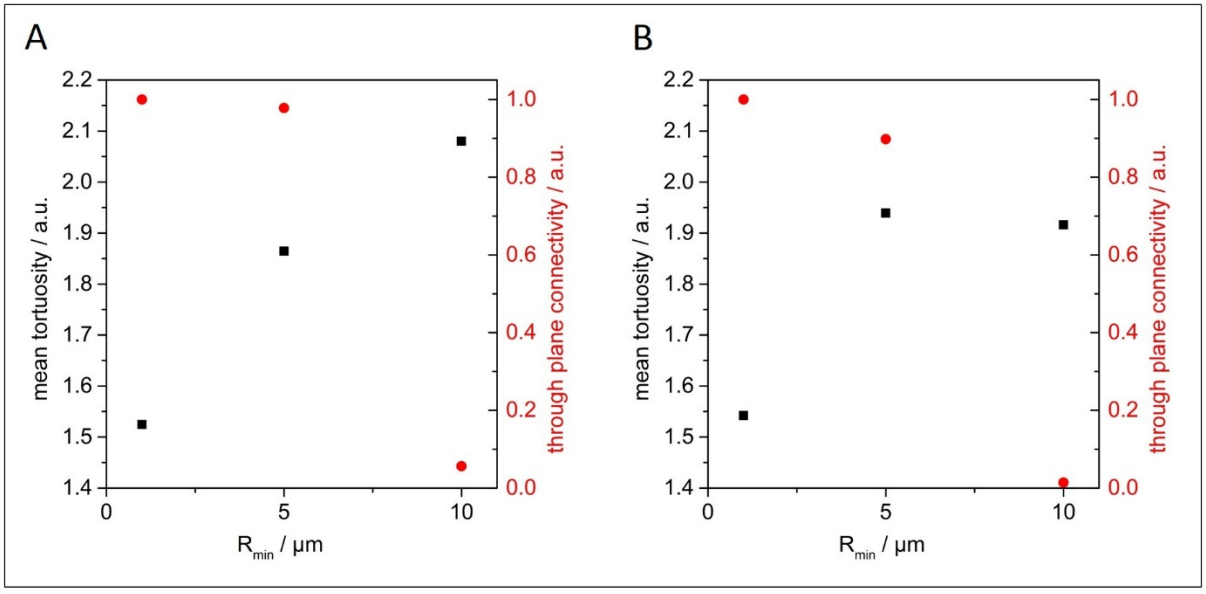

Figure 7. Mean geometric tortuosity at different radius limitations R_{min} of percolation paths (black rectangles) and the respective through-plane connectivity (red circles) A: degree of compression = 0 vol.%; B: degree of compression = 31 vol.%.

3.2. Inhomogeneous GDL compression by the flow field pattern

When assembled in fuel cells, GDLs are inhomogeneously loaded and compressed by the channel-land-pattern of the flow-field. In this section, we adapt the sample compression to more realistic conditions using a compression punch with an integrated channel-land profile. Figure 8 shows perspective views on the GDL sample which has successively been compressed. The initial thickness $Z_0 = 219$ has been reduced to $Z_{10} = 197$ µm, $Z_{20} = 180$ µm, $Z_{30} = 155$ µm which refers to actual compression rates of 10 vol.%, 18 vol.%, and 29 vol.%. The reconstructed image volume was cut to provide a cross sectional insight. In this perspective, it is clearly visible how the contour of the compressing tool is stamped into the GDL with increasing compression, eventually generating considerable differences in the local material density. While the material underneath the land is homogenously compressed to the thickness determined by the compression device the fiber structure underneath the channel is much less and inhomogeneously compressed. The material thickness along the center line of the channel remains almost constant. This implies that upon assembly in fuel cells the fiber material significantly extends into the channel volume and occupies space at the expense of the media flow capacity of the channel. Figure 8 also exhibits some individual fiber endings that are bent up by the channel edges. These fiber endings interfere with the gas flow inside the channel and could even alter the flow regime, e.g. by producing vortexes or by hampering

the passage of water droplets. As those fibers can hold up moving droplets they are potential accumulation points for liquid water in the channel.

We investigated the influence of the flow-field geometry on the local GDL morphology by calculating geometrical parameters relevant for transport for regions located underneath both channels and land. In the following we refer to these regions as “land region” and “channel region”, respectively. Figure 9 illustrates the size and position of the analyzed GDL sub-regions. The dimensions of the two land regions are 219 × 1314 × z µm^3, respectively, where parameter z denotes the thickness, which is adjusted to the increasing compression: z is 192 µm, 171 µm, 158 µm and 131 µm. In contrast to land areas, the local thickness of the GDL material in the channel region strongly depends on the distance to the channel edge. The maximum thickness is found at the channel center from where it continuously decreases towards the land area. With increasing sample compression, the thickness at the center remains almost constant or even slightly increases (see below for more details), whereas fiber material closer to the channel edges is increasingly compressed. We analyzed geometric properties of the channel region within a sub-volume of 701 × 1314 × 245 µm^3 (x × y × z) which was thoroughly filled with GDL material for all the compression stages under study.

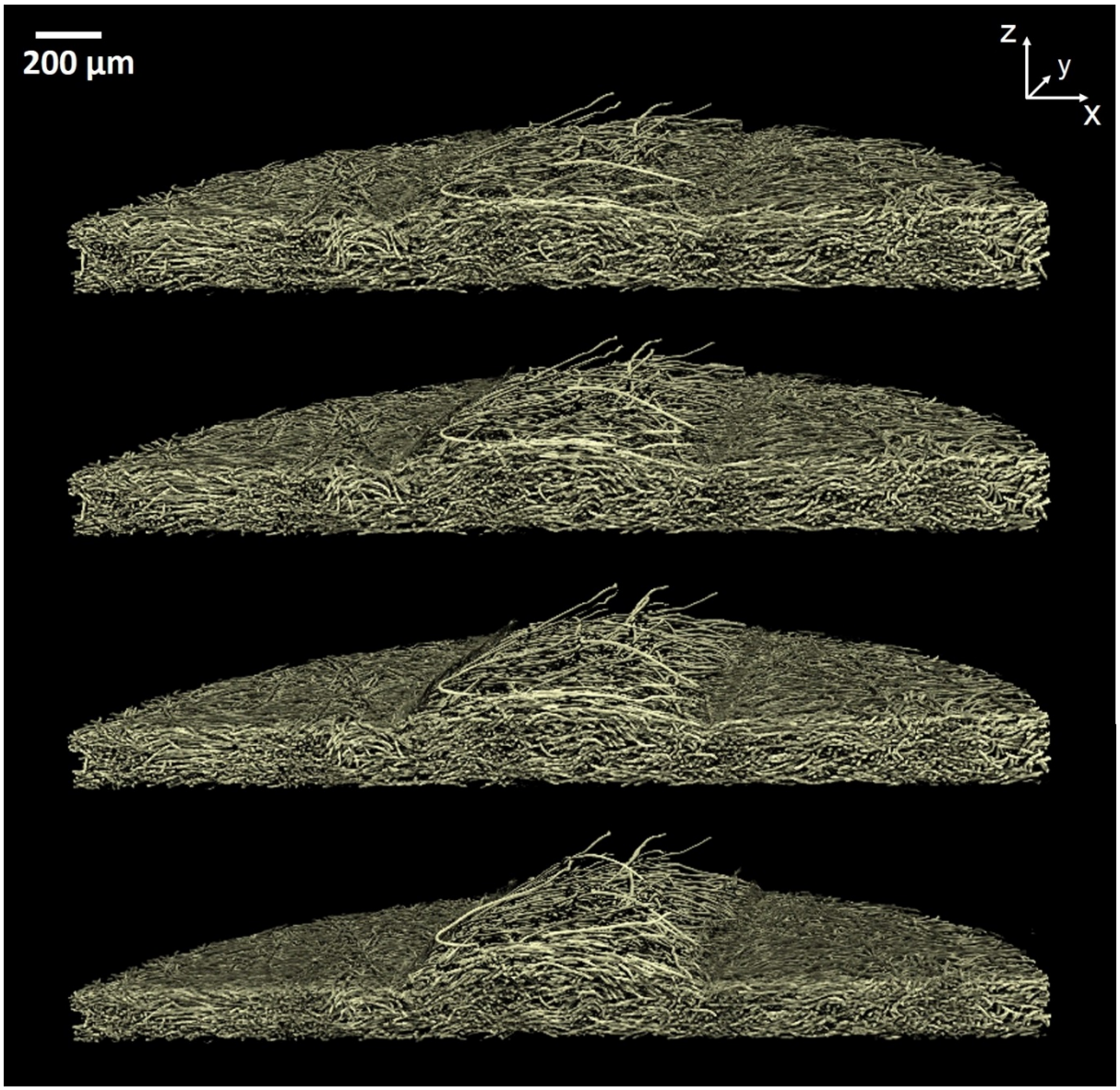

Figure 8. Nonwoven GDL sample compressed by a channel-land profile. Compression underneath land area is (from top to bottom) 0 vol.%, 10 vol.%, 18 vol.%, and 29 vol.%.

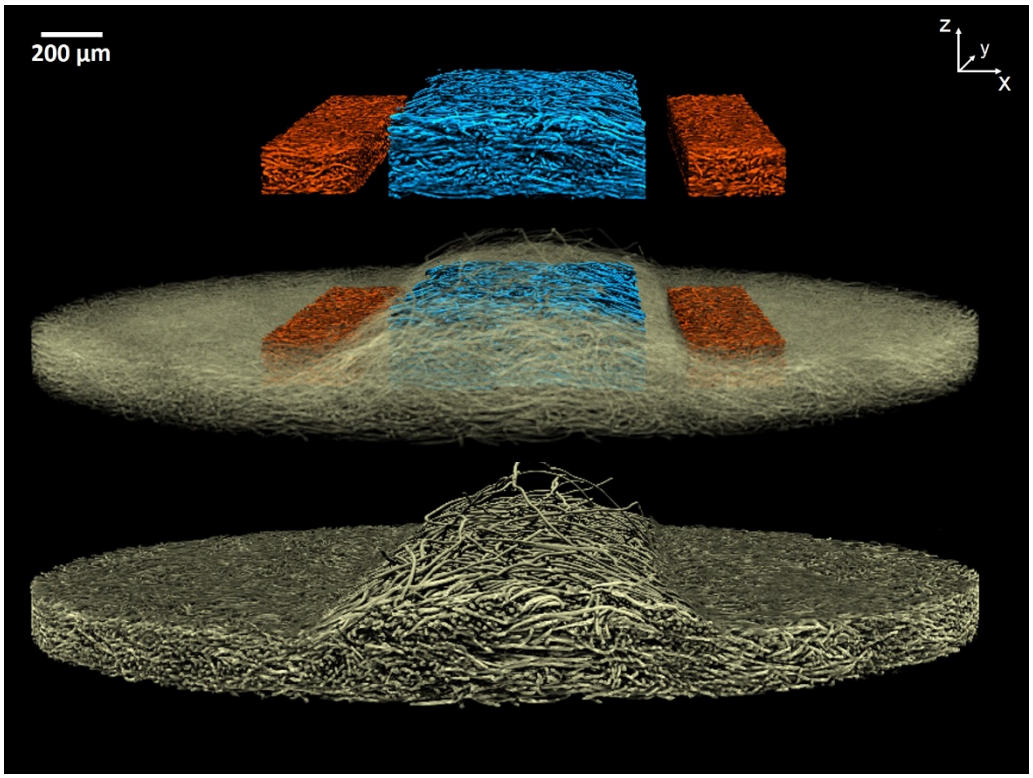

Figure 9. Visualization of GDL sub-volumes analyzed: Illustration of size and position within the sample (degree of compression 29 vol.%). The land regions are highlighted in red, the channel region in blue.

The porosity of the GDL within both land and channel region at different degrees of compression is displayed in figure 10. The difference in porosity between the two areas in the uncompressed state is due to the precompression of the sample during preparation as explained in section 3.1. The porosity underneath the land decreases according to the reduction of the pore volume by the compression punch very similar to the results of the flat punch shown in figure 4a. In contrast, underneath the flow-field channel, were the GDL material is not in direct contact with the compression punch, the porosity decreases only slightly. This is in good accordance with the visual impression of the morphology provided by figure 8.

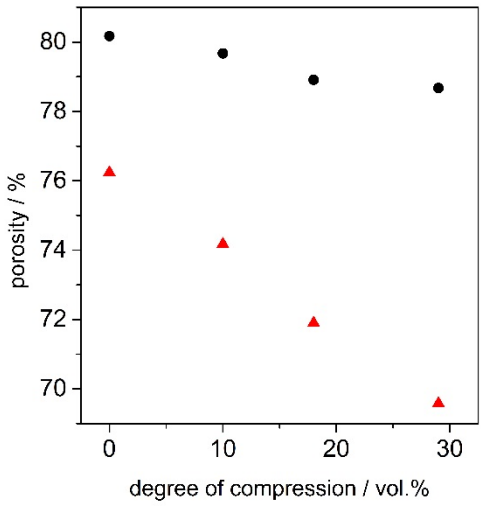

Figure 10. Porosity determined for land (red triangles) and channel areas (black dots) at different rates of compression.

In order to study the pore phase in more detail the continuous PSD is calculated for both the land and channel regions. A plot of the cPSD is presented in figure 11. Underneath the land the graphs of cPSD are equivalent to those calculated for the homogenous compression by the flat punch. Comparison of the results for channel and land regions shows that the channel region contains a notable amount of pores with a radius > 30 µm, whereas no pores of this size are present underneath the land area. When focusing on radii ≥ 30 µm in figure 11a we find that the pore volume inside the channel region slightly increases with compression. This seemingly paradox can be explained by the concave deformation of fiber material underneath the channel. The bending stress exerted at the channel edges slightly bows the GDL material. Consequently, pores located in the top layers of the sample are stretched while those located in the bottom layers are slightly compressed which results in an almost constant overall porosity of the channel region considered.

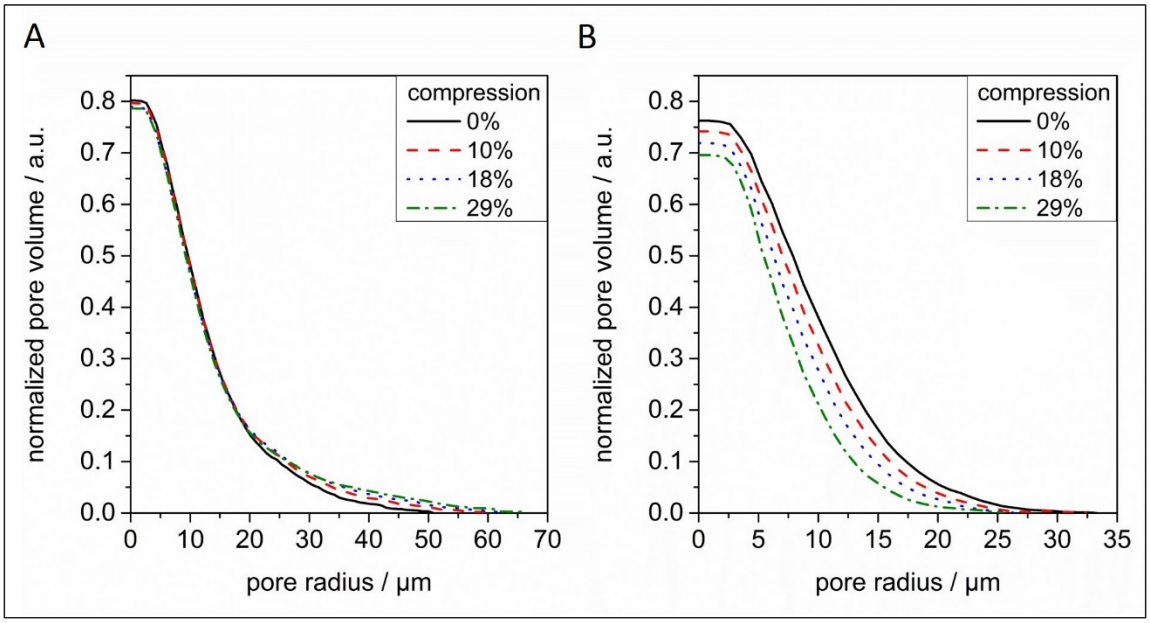

Figure 11. Continuous pore size distribution computed for channel (A) and land regions (B).

Figure 12 shows the influence of inhomogeneous compression on the local GDL thickness and the partial occupation of the flow-field channel by the fiber material. The plot of the sample thickness measured at the channel center and underneath the land at different degrees of compression reveals that the GDL is much less compressed in the channel region. While the thickness beneath the land is successively reduced by 10, 18 and 29% by the compression punch, it even increases slightly at the center line of the flow-field channel. At 29% compression the GDL is twice as thick along the center line of the channel as in the land region. Consequently, it extends far into the channel volume as displayed in figure 12b. Already in the uncompressed state a penetration depth of 90 µm is measured for the GDL. With increasing degree of compression the material continues to extend into the channel. At 29% compression the penetration depth reaches 167 µm. Figure 12c also clearly demonstrates that individual fiber endings protrude into the flow-field channel. These fibers are bent at the edges of the flow-field channel profile and tilt up with increasing degree of compression. At a compression degree of 29% some fiber endings protrude 295 µm into the channel volume where they potentially influence the gas flow and form obstacles for water droplets that are transported through the flow field channel.

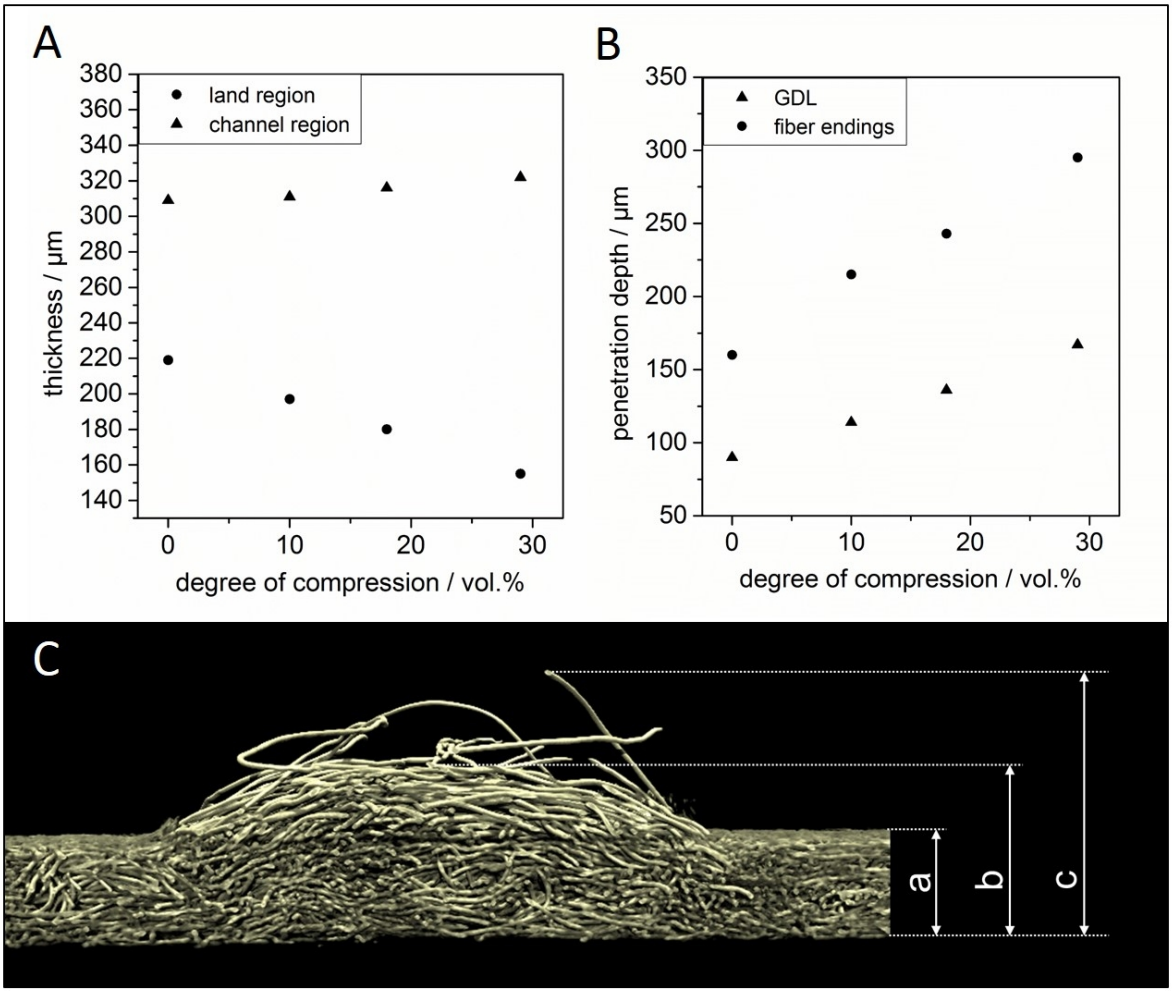

Figure 12: Evaluation of GDL thickness underneath land and channel areas. A) Plot of GDL thickness underneath land (circles) and channel (triangles). B) Plot of the penetration depth of GDL (triangles) and outermost fibers (circles) into the channel volume. C) Perspective side-view illustrating the thickness of the GDL sample at a compression rate of 29%. a= thickness underneath land; b= thickness underneath channel; c=thickness including the most distant fiber ends; b-a=penetration depth of GDL into channel; c-a= penetration depth of outermost fiber ends.

4. Conclusions

Synchrotron X-ray tomography was used to study the microstructure of carbon fiber-based GDL materials at different degrees of compression. A dedicated compression device was used to provide realistic compression conditions that reflect conditions in real fuel cells. The application of different compression punches allowed for studying geometric properties relevant for the transport of media in homogenously compressed GDL material as well as to investigate the influence of the land-channel-pattern of the flow field on the local microstructure of the GDL. The main findings of the tomographic study are:

1. The geometric properties of the fiber-based material are altered significantly upon compression. This has a direct impact on the transport conditions for both gas and fluid flow in the GDL.
2. Compression mainly affects the pores while the fibers are almost incompressible.
3. When homogenously compressed, fibers are mainly translated in the *z*-direction.
4. Depending on the degree of compression the pore volume mainly consist of pores with a radius ranging between 5 µm and 15 µm.
5. We found only a minor influence of compression on the geometric tortuosity in through-plane direction.
6. Taking into account the transport limiting effect of bottlenecks (radius constrictions along the 3D transport paths) the mean tortuosity of the uncompressed material increases from about 1.5 to about 2.1 when only 3D paths with a minimal radius of at least 10 µm are included in the calculation. Only a few percent of the possible transport paths through the GDL fulfill this criterion but that very paths might act as preferred water transport channels from the catalyst layer to the channel. This result is in agreement with recent findings from in-operando studies by Markötter et al. [8, 40].
7. The through-plane connectivity of transport paths that satisfy the bottleneck criterion strongly depends on the minimum pore radius as well as on the degree of compression. A compression of 31 vol.% decreases the number of available broad 3D transport paths with a minimum diameter of at least 20 µm to 25% of the initial value (see figure 7b). These broad paths are most important for liquid water transport. Therefore, compression causes a significant decrease of low resistance water transport paths.
8. Compression of the fiber structure by the flow-field strongly alters the overall GDL structure. While homogeneously compressed underneath the land it is much less and inhomogeneously compressed underneath a flow-field channel. At the center of flow field channels even a local increase in porosity might occur due to the pronounced extension of fiber layers into the channel volume.
9. The fiber material extends far into the flow-field channel volume and occupies channel volume that is actually provided for gas flow and removal of liquid water. For example, a penetration depth of 167 µm was measured for a compression of 29 vol.%.
10. We found many fibers tilted up by bending stresses at channel edges with their endings penetrating deeply into the flow field channel. For example, a penetration depth of 295 µm was measured for a compression of 29 vol.%. This can have significant influence on both the gas and liquid flow as those fibers form obstacles for

moving water droplets and can potentially create agglomerations of liquid water in the fuel cell. This effect has also to be taken into account in future flow field simulations.

5. Outlook

In this study, the superior brilliance of a synchrotron X-ray beam and the high spatial resolution of the associated imaging instrument were exploited to generate tomographic data that reproduce even smallest morphological details of the fiber material with great accuracy. This information was used to estimate some effects of the microstructure on both gas and liquid transport. However, a more detailed analysis of water and gas transport properties of the GDL material additionally requires numerical transport computations, e.g. by Lattice-Boltzmann simulations. The accuracy of such transport simulations significantly relies on the quality of geometric structure models and the implementation of realistic boundary conditions. When simulating water and gas transport through the GDL, the geometry of the inhomogeneously compressed gas diffusion layer should be carefully taken into account. This is especially important when it comes to computing mass and energy transfer from the GDL into the flow-field channel. The highly resolved tomographic data produced in this study is considered a valuable source of information for defining appropriate boundary conditions and is ideally suited as experimental basis for the development of stochastic microstructure models needed for the design of materials with improved functionality by means of computer experiments.

Acknowlegdements

We gratefully acknowledge funding of the present research by the German Federal Ministry for Education and Science (BMBF) under grant numbers 05M10KTA, 05M10CJA, 05M10VUA, and 05M10DAA.

References

[1] C.-Y. Wang, Chemical Reviews, 104 (2004) 4727-4766.
[2] L. Carrette, K.A. Friedrich, U. Stimming, Fuel Cells, 1 (2001) 5-39.
[3] C. Hartnig, L. Jörissen, J. Scholta, W. Lehnert, Gas diffusion media, flowfields and system aspects in low temperature fuel cells, in: C. Hartnig, C. Roth (Eds.) Fundamentals and performance of low temperature fuel cells, Woodhead Publishing Limited, 2012, pp. 81-116.
[4] U. Pasaogullari, C.-Y. Wang, Journal of The Electrochemical Society, 152 (2005) A380-A390.
[5] C. Ziegler, H.M. Yu, J.O. Schumacher, Journal of The Electrochemical Society, 152 (2005) A1555-A1567.

[6] C.Y. Wang, P. Cheng, International Journal of Heat and Mass Transfer, 39 (1996) 3607-3618.
[7] P.K. Sinha, P.P. Mukherjee, C.Y. Wang, Journal of Materials Chemistry, 17 (2007) 3089-3103.
[8] P. Zhou, C.W. Wu, Journal of Power Sources, 195 (2010) 1408-1415.
[9] A. Bazylak, D. Sinton, N. Djilali, Journal of Power Sources, 176 (2008) 240-246.
[10] S. Litster, D. Sinton, N. Djilali, Journal of Power Sources, 154 (2006) 95-105.
[11] N. Kardjilov, I. Manke, A. Hilger, M. Strobl, J. Banhart, Materials Today, 14 (2011) 248-256.
[12] M. Strobl, I. Manke, N. Kardjilov, A. Hilger, M. Dawson, J. Banhart, Journal of Physics D-Applied Physics, 42 (2009).
[13] I. Manke, H. Markötter, C. Tötzke, N. Kardjilov, R. Grothausmann, M. Dawson, C. Hartnig, S. Haas, D. Thomas, A. Hoell, C. Genzel, J. Banhart, Advanced Engineering Materials, 13 (2011) 712-729.
[14] S.R. Stock, International Materials Reviews, 53 (2008) 129-181.
[15] J.P. James, H.W. Choi, J.G. Pharoah, International Journal of Hydrogen Energy, 37 (2012) 18216-18230.
[16] J. Becker, R. Flückiger, M. Reum, F.N. Büchi, F. Marone, M. Stampanoni, Journal of The Electrochemical Society, 156 (2009) B1175-B1181.
[17] R. Flückiger, F. Marone, M. Stampanoni, A. Wokaun, F.N. Büchi, Electrochimica Acta, 56 (2011) 2254-2262.
[18] R.J. Bellows, M.Y. Lin, M. Arif, A.K. Thompson, D. Jacobson, Journal of The Electrochemical Society, 146 (1999) 1099-1103.
[19] R. Satija, D.L. Jacobson, M. Arif, S.A. Werner, Journal of Power Sources, 129 (2004) 238-245.
[20] M.A. Hickner, N.P. Siegel, K.S. Chen, D.S. Hussey, D.L. Jacobson, M. Arif, Journal of The Electrochemical Society, 155 (2008) B427-B434.
[21] A.B. Geiger, A. Tsukada, E. Lehmann, P. Vontobel, A. Wokaun, G.G. Scherer, Fuel Cells, 2 (2002) 92-98.
[22] P. Boillat, D. Kramer, B.C. Seyfang, G. Frei, E. Lehmann, G.G. Scherer, A. Wokaun, Y. Ichikawa, Y. Tasaki, K. Shinohara, Electrochemistry Communications, 10 (2008) 546-550.
[23] N. Pekula, K. Heller, P.A. Chuang, A. Turhan, M.M. Mench, J.S. Brenizer, K. Ünlü, Nuclear Instruments and Methods in Physics Research Section A: Accelerators, Spectrometers, Detectors and Associated Equipment, 542 (2005) 134-141.
[24] P.K. Sinha, P. Halleck, C.-Y. Wang, Electrochemical and Solid-State Letters, 9 (2006) A344-A348.
[25] I. Manke, C. Hartnig, N. Kardjilov, H. Riesemeier, J. Goebbels, R. Kuhn, P. Krüger, J. Banhart, Fuel Cells, 10 (2010) 26-34.
[26] I. Manke, C. Hartnig, M. Grunerbel, W. Lehnert, N. Kardjilov, A. Haibel, A. Hilger, J. Banhart, H. Riesemeier, Applied Physics Letters, 90 (2007) 174105.
[27] C. Hartnig, I. Manke, R. Kuhn, S. Kleinau, J. Goebbels, J. Banhart, Journal of Power Sources, 188 (2009) 468-474.
[28] P. Krüger, H. Markötter, J. Haußmann, M. Klages, T. Arlt, J. Banhart, C. Hartnig, I. Manke, J. Scholta, Journal of Power Sources, 196 (2011) 5250-5255.
[29] G. Gaiselmann, D. Froning, C. Tötzke, C. Quick, I. Manke, W. Lehnert, V. Schmidt, International Journal of Hydrogen Energy, 38 (2013) 8448-8460.
[30] G. Gaiselmann, R. Thiedmann, I. Manke, W. Lehnert, V. Schmidt, Computational Materials Science, 59 (2012) 75-86.
[31] R. Thiedmann, C. Hartnig, I. Manke, V. Schmidt, W. Lehnert, Journal of the Electrochemical Society, 156 (2009) B1339-B1347.
[32] K. Seidenberger, F. Wilhelm, J. Haußmann, H. Markötter, I. Manke, J. Scholta, Journal of Power Sources, 239 (2013) 628-641.
[33] J.P. Brinkmann, D. Froning, U. Reimer, V. Schmidt, W. Lehnert, D. Stolten, ECS Transactions, 50 (2013) 207-219.
[34] W. Görner, M.P. Hentschel, B.R. Müller, H. Riesemeier, M. Krumrey, G. Ulm, W. Diete, U. Klein, R. Frahm, Nuclear Instruments and Methods in Physics Research Section A: Accelerators, Spectrometers, Detectors and Associated Equipment, 467-468 (2001) 703-706.
[35] S.H. Williams, A. Hilger, N. Kardjilov, I. Manke, M. Strobl, M.P.A. Douissard, T. Martin, H. Riesemeier, J. Banhart, Journal of Instrumentation, 7 (2012) P02014.
[36] A. Heinzel, G. Bandlamudi , W. Lehnert, in: J. Garche, C.K. Dyer, P.T. Moseley, Z. Ogumi, D.A.J. Rand, B. Scrosati (Eds.) Encyclopia of Electrochemical Power Sources, Elsevier, 2009.
[37] C. Wannek, W. Lehnert, J. Mergel, Journal of Power Sources, 192 (2009) 258-266.
[38] W. Maier, T. Arlt, K. Wippermann, C. Wannek, I. Manke, W. Lehnert, D. Stolten, Journal of The Electrochemical Society, 159 (2012) F398-F404.
[39] B. Münch, L. Holzer, Journal of the American Ceramic Society, 91 (2008) 4059-4067.
[40] H. Markötter, I. Manke, P. Krüger, T. Arlt, J. Haussmann, M. Klages, H. Riesemeier, C. Hartnig, J. Scholta, J. Banhart, Electrochemistry Communications, 13 (2011) 1001-1004.